



Generation of shear flows and vortices in rotating anelastic convection

Laura K. Currie ^{*}*Department of Mathematics and Computer Science, College of Engineering, Mathematics and Physical Sciences, University of Exeter, Exeter EX4 4QF, United Kingdom*Steven M. Tobias [†]*Department of Applied Mathematics, University of Leeds, Leeds LS2 9JT, United Kingdom*

(Received 3 December 2019; accepted 3 June 2020; published 8 July 2020)

We consider the effect of stratification on systematic large-scale flows generated in anelastic convection. We present results from three-dimensional numerical simulations of convection in a rotating plane layer in which the angle between the axis of rotation and gravity is allowed to vary. This model is representative of different latitudes of a spherical body. We consider two distinct parameter regimes: (i) weakly rotating and (ii) rapidly rotating. In each case, we examine the effect of stratification on the flow structure and heat transport properties focusing on the difference between Boussinesq and anelastic convection. Furthermore, we show that regimes (i) and (ii) generate very different large-scale flows and we investigate the role stratification has in modifying these flows. The stratified flows possess a net helicity not present in the Boussinesq cases which we suggest, when combined with the self-generated shear flows, could be important for dynamo action.

DOI: [10.1103/PhysRevFluids.5.073501](https://doi.org/10.1103/PhysRevFluids.5.073501)

I. INTRODUCTION

Fluid turbulence is known to interact nontrivially with rotation to drive systematic flows. The presence of rotation can lead to the breaking of the parity symmetry of the turbulent system and also to the presence of a pseudoscalar that naturally leads to the establishment of mean flows. In geophysical and astrophysical fluids, systematic flows coexisting with turbulence on a vast range of spatial and temporal scales are often observed. Examples include the differential rotation of the solar interior [1], the systematic banded zonal jets and polar vortices visible at the surface of the gas giants [2–4], and the strong flows driven in Earth’s atmosphere and oceans [5]. An important question is to identify the role of correlations in the turbulence in driving the mean flows *and* the backreaction of the mean flows on the statistics of the turbulence that leads to the self-consistent saturation of such flows.

In many, though certainly not all, cases of interest the turbulent flow is driven by buoyancy forces and arises as thermal or compositional convection. The convective turbulence naturally interacts with rotation to drive mean flows, which themselves play a role in mediating the heat transport. This interaction is complicated and can even lead to such complicated dynamics as predator-prey bursting where the solution oscillates between strong mean flows and efficient convection [6–8].

There have been many previous studies of the interaction of convection with large-scale systematic flows, owing to its key role in the dynamics of planetary and stellar interiors. These studies have employed a variety of techniques including direct numerical simulation (DNS) [9,10],

^{*}L.K.Currie@exeter.ac.uk

[†]S.M.Tobias@leeds.ac.uk

turbulence closure models [11, 12], or direct statistical simulation [13–15]. Investigations have been performed in both spherical geometry [9, 16–24] and local Cartesian models [25–31]. There is also a class of intermediate local models that captures some of the effects of the vortex stretching engendered by the spherical geometry by use of an annulus geometry [32–34].

In this paper we study the interaction of convection and systematic flows in a local Cartesian model. Such a model lacks some of the geometrical effects of the global spherical models, but allows for a higher degree of turbulence and for more rapid rotation than the more computationally demanding spherical models. The previous studies investigating the interaction of convection with systematic flows have predominantly been carried out utilizing the Boussinesq approximation [35, 36], which is a good approximation when the density variations are relatively unimportant. This is the case for some (though not all) planetary interiors; for example, in the Earth’s core the density varies by only approximately 20% from the inner core boundary to the core-mantle boundary [37]. This translates to a number of density scale heights N_ρ of 0.18. By contrast, Jupiter’s deep interior has a density contrast characterized by $N_\rho \sim 5$ [38, 39] and so the Boussinesq approximation should be deemed less appropriate to this case. Similarly, density variations can also play an important role in the interior of stars (the convection zone of the Sun encompasses approximately 14 density scale heights [40–42]).

Relevant Boussinesq models include asymptotic models of rapidly rotating convection in a plane layer [28], DNS of convection in layers with tilted rotation vectors and no slip [25] or stress-free boundary conditions [43], and the interaction of convection with an imposed shear flow [27, 29]. Furthermore, Currie [44] examined the generation of mean flows by Reynolds stresses in Boussinesq convection both in the absence and in the presence of a thermal wind and highlighted the importance of the fluid Prandtl number and the angle of the rotation vector from the vertical for determining the dynamics.

In this paper we focus on the important role of stratification in determining the form of the convection and the associated flows. Currie and Tobias [30] considered the effect of stratification on mean flow generation in two-dimensional anelastic convection in a rotating plane layer. Here we extend that investigation to three dimensions and probe a larger range of rotation rates. The anelastic approximation allows the filtering of sound waves while still retaining the effects of density stratification and so gives a computationally efficient framework for studying the role of stratification and its interaction with rotation. Although fully compressible local models with rotation have been studied in the past [45–47], the local dynamics of anelastic convection is comparatively poorly studied and understood. However, we note that the anelastic framework has previously been utilized to model penetrative convection [48] and for nonrotating two-dimensional (2D) systems [49]. Moreover, Verhoeven and Stellmach [50] performed 2D anelastic simulations of rapidly rotating convection in the equatorial plane (gravity and rotation perpendicular). More recently, Kessar *et al.* [51] examined the role of stratification in determining the length scales of turbulent convection using 3D simulations of nonrotating anelastic convection in a Cartesian layer.

The main focus of this paper then is in determining the role of stratification in modifying interactions between large-scale shear flows (or vortices) and convection driven turbulence. The paper is organized as follows. In Sec. II we present the model and governing equations. In Sec. III we consider the effects of stratification on convection in two distinct regimes: (i) weakly rotating and (ii) rapidly rotating. In addition, we investigate the effect of stratification on large-scale flows that are self-consistently generated by the convection and discuss the potential of such flows to act as dynamos. We summarize in Sec. IV.

II. MODEL SETUP AND EQUATIONS

We consider a Cartesian plane layer of convecting fluid rotating about an axis that is oblique to gravity, which acts downward. The rotation axis lies in the y - z plane and is given by $\boldsymbol{\Omega} = (0, \Omega \cos \phi, \Omega \sin \phi)$, where Ω is the rotation rate and ϕ is the angle of the tilt of the rotation vector from the horizontal, so that the layer can be interpreted as being tangent to a sphere at a latitude ϕ .

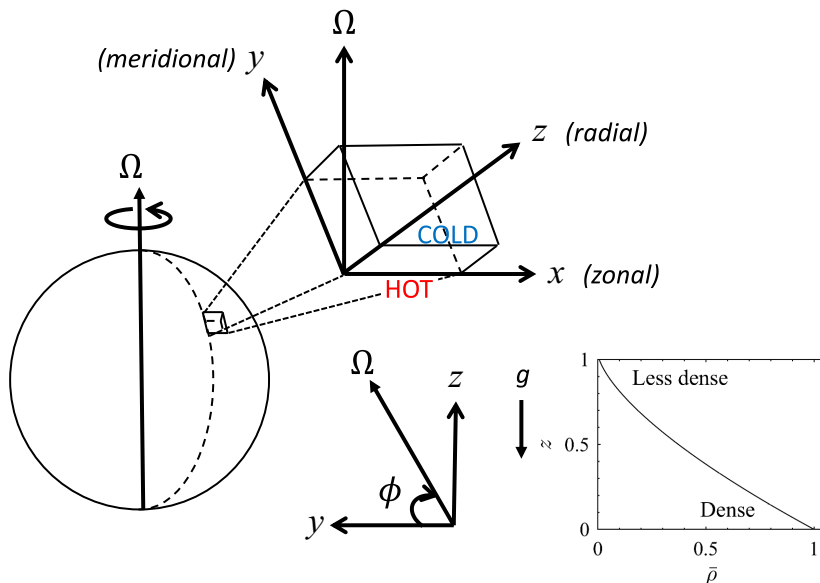


FIG. 1. Geometry. The simulation domain is taken to be a Cartesian plane layer, located at a latitude ϕ on a spherical body. The rotation axis lies in the y - z plane and is given (for a rotation rate Ω) by $\mathbf{\Omega} = (0, \Omega \cos \phi, \Omega \sin \phi)$. The z axis points upward, the x axis eastward, and the y axis northward. Gravity acts downward. The axes on the right-hand side show the background density stratification $\bar{\rho}(z)$ for a strongly stratified system where the fluid is much denser at the bottom of the layer than at the top.

We take the z axis to point upward, the x axis eastward, and the y axis northward (see Fig. 1). Note we choose the z axis to point upward for ease of comparison with Boussinesq models where the vertical axis increases upward; this is in contrast to many compressible studies where it is taken to point downward.

The anelastic equations are found by decomposing the density ρ , pressure p , and temperature T of the fluid into an almost adiabatic reference state (denoted by an overbar) and a perturbation (denoted by a prime):

$$\rho = \rho_0(\bar{\rho} + \epsilon\rho'), \quad p = p_0(\bar{p} + \epsilon p'), \quad T = T_0(\bar{T} + \epsilon T'). \quad (1)$$

The entropy is expanded as $s = \text{const} + \epsilon c_p(\bar{s} + s')$, where c_p is the specific heat capacity at constant pressure. Here quantities with a subscript 0 are reference values of the corresponding quantities taken at the bottom of the layer, $z = 0$. In addition, ϵ is a measure of the departure of the reference state from adiabaticity, defined as

$$\epsilon \equiv \frac{d}{H_0} \left(\frac{\partial \ln \bar{T}}{\partial \ln \bar{p}} - \frac{\partial \ln \bar{T}}{\partial \ln \bar{p}} \Big|_{\text{ad}} \right) = -\frac{d}{T_0} \left[\left(\frac{d\bar{T}}{dz} \right)_0 + \frac{g}{c_p} \right] = -\frac{d}{c_p} \left(\frac{d\bar{s}}{dz} \right)_0 \ll 1, \quad (2)$$

where d is the layer depth, $H = \frac{\bar{p}}{g\rho}$ is the pressure scale height, and g is the acceleration due to gravity. We assume an ideal gas so that $p = \mathcal{R}\rho T$ (where \mathcal{R} is the universal gas constant); the entropy of the ideal gas is then given by $s = \text{const} + c_v \ln(\frac{p}{\rho^\gamma})$, where c_v is the specific heat capacity at constant volume. Note that the constant in the definition of s can be conveniently chosen so that $s = 0$ on the upper boundary.

The anelastic governing equations (see, for example, [52–55]) for a fluid with velocity $\mathbf{u} = (u, v, w)$ can then be written as

$$\left[\frac{\partial \mathbf{u}}{\partial t} + (\mathbf{u} \cdot \nabla) \mathbf{u} \right] = -\nabla \left(\frac{p}{\bar{\rho}} \right) + \text{Ra Pr} S \hat{\mathbf{e}}_z - \text{Ta}^{1/2} \text{Pr} \boldsymbol{\Omega} \times \mathbf{u} + \frac{\text{Pr}}{\bar{\rho}} \nabla \cdot \boldsymbol{\zeta}, \quad (3)$$

$$\nabla \cdot (\bar{\rho} \mathbf{u}) = 0, \quad (4)$$

$$\bar{\rho} \bar{T} \left[\frac{\partial S}{\partial t} + (\mathbf{u} \cdot \nabla) S \right] = \nabla \cdot [\bar{T} \nabla S] - \frac{\theta}{\bar{\rho} \text{Ra}} \frac{\boldsymbol{\zeta}^2}{2}, \quad (5)$$

where we have removed the primes from the perturbation quantities. In this formalism, we have assumed that the kinematic viscosity and the thermal conductivity do not vary with depth; this is discussed further below. Note that because the reference state is close to adiabatic it is not necessary to introduce a separate perturbation to the entropy and so we instead solve for the total entropy $S = \bar{s} + s'$. The full thermodynamic state can then be obtained from the anelastic versions of the equation of state and entropy definition, respectively:

$$\frac{p}{\bar{p}} = \frac{T}{\bar{T}} + \frac{\rho}{\bar{\rho}}, \quad (6)$$

$$S = \frac{1}{\gamma} \frac{p}{\bar{p}} - \frac{\rho}{\bar{\rho}}. \quad (7)$$

Equations (3)–(7) are written in a dimensionless form, where we have scaled the dimensional equations using d as the unit of length and the thermal diffusion time d^2/κ_0 as the unit of time (κ_0 is the value of the thermal diffusivity at the bottom of the layer). Here $\boldsymbol{\zeta}$ is the stress tensor defined by $\zeta_{ij} = \bar{\rho} \left[\frac{\partial u_i}{\partial x_j} + \frac{\partial u_j}{\partial x_i} - \frac{2}{3} (\nabla \cdot \mathbf{u}) \delta_{ij} \right]$, with $\boldsymbol{\zeta}^2 \equiv \boldsymbol{\zeta} : \boldsymbol{\zeta} = \zeta_{ij} \zeta_{ij}$; θ is the dimensionless temperature difference across the layer and γ is the ratio of specific heats at constant pressure to constant volume. For convenience, we have introduced the dimensionless parameters

$$\text{Ra} = \frac{gd^3\epsilon}{\kappa_0\nu}, \quad \text{Ta} = \frac{4\Omega^2 d^4}{\nu^2}, \quad \text{Pr} = \frac{\nu}{\kappa_0}, \quad (8)$$

commonly known as the Rayleigh, Taylor, and Prandtl numbers, respectively. Here ν is the kinematic viscosity which does not vary with depth in this model.

We consider a time-independent polytropic reference state given by

$$\begin{aligned} \bar{T} &= 1 + \theta z, & \bar{\rho} &= (1 + \theta z)^m, & \bar{p} &= -\frac{\text{Ra Pr}}{\theta(m+1)} (1 + \theta z)^{m+1}, \\ \bar{s} &= \frac{m+1-\gamma m}{\gamma\epsilon} \ln(1 + \theta z) + \text{const} & \text{with } \frac{m+1-\gamma m}{\gamma} &= -\frac{\epsilon}{\theta} = O(\epsilon), \end{aligned} \quad (9)$$

where m is the polytropic index, which we take to be 1.5 throughout this article, and $-1 < \theta \leq 0$. We note in this model that the reference state is independent of time and so there is no adjustment by any mean that may be generated. The functional form of the background density stratification $\bar{\rho}$ for a density contrast (between the top and bottom of the layer) of approximately 150 is shown in Fig. 1.

Note that, within the anelastic approximation, for a stratified layer one cannot take both the dynamic viscosity μ and the kinematic viscosity ν of the fluid to be constant; at least one must be depth dependent (since $\mu = \bar{\rho}\nu$). Similarly, one cannot take both the thermal conductivity k and the thermal diffusivity κ of the fluid to be constant and so there is some freedom over which parameters are kept constant across the layer depth and which vary. The results can depend on these choices (see, e.g., [56]). In our formalism, we assume ν and $k = \bar{\rho}c_p\kappa$ (where we interpret κ as the turbulent thermal diffusivity) to be constant (and therefore μ and κ must vary with depth). While the overall Rayleigh and Prandtl numbers quoted in this article are defined at the bottom of the layer [as given

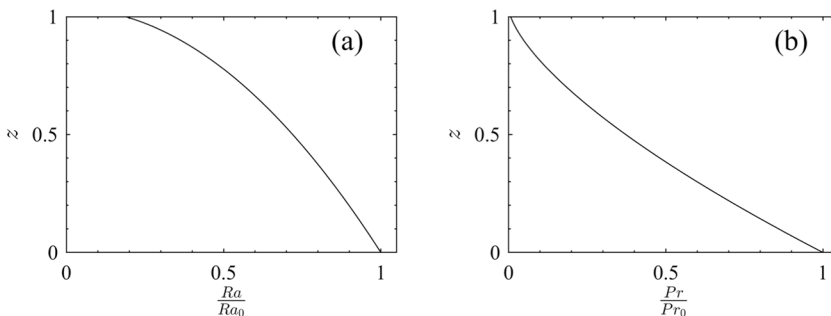


FIG. 2. Depth-dependent (a) Rayleigh and (b) Prandtl numbers as given by (10). They are shown for $\theta = -0.96433$ ($N_\rho = 5$) and have been normalized by the value on the bottom boundary.

in (8)], we can also define analogous depth-dependent dimensionless parameters $Ra(z)$ and $Pr(z)$ and these can vary significantly with depth at strong stratifications (note that Ta is constant across the depth). In particular, we have

$$Ra(z) = Ra_0(1 + \theta z)^{m-1}, \quad Pr(z) = Pr_0(1 + \theta z)^m. \quad (10)$$

We note that, for no stratification, $\theta = 0$ and Ra and Pr are constant across the layer. Figure 2 shows the variation in $Ra(z)$ and $Pr(z)$ across the layer for a density contrast of approximately 150 between the top and bottom of the layer ($\bar{\rho}$ for this case is shown in Fig. 1). It is clear that both Ra and Pr are significantly smaller at the top of the domain than at the bottom in strongly stratified cases. This will have significant consequences for the form of the convection and will be discussed further in Sec. III A.

Anelastic formalisms also differ depending on whether entropy or temperature is diffused in the energy equation [53]. We choose a model that takes the turbulent thermal conductivity to be much larger than the molecular conductivity and so Eq. (5) contains an entropy diffusion term but not a thermal diffusion term; Braginsky and Roberts [53] discuss models including both terms. In choosing to diffuse entropy, temperature can be eliminated as a variable from the formulation using a technique introduced by Lantz [52] and Braginsky and Roberts [53] (see also the work of Lantz and Fan [54] and Jones and Kuzanyan [57]).

Equations (3)–(7) along with the reference state (9) are similar to those given in case (1) of Mizerski and Tobias [55] but here the rotation vector has been generalized to include cases where the rotation vector and gravity are not aligned, i.e., $\mathbf{\Omega} = (0, \cos \phi, \sin \phi)$. Currie and Tobias [30] solved the 2.5D version of these equations, i.e., the version with all three velocity components, but with a dependence of all variables only on y and z . In this particular formalism, the anelastic equations (3)–(7) reduce to the Boussinesq equations in the limit $\theta \rightarrow 0$ and so θ can be thought of as a measure of the degree of compressibility. However, we choose instead to use the number of density scale heights in the layer N_ρ as a measure of the stratification. Here N_ρ is related to θ through $N_\rho = \ln(1 + \theta)^{-m}$; it can also be expressed in terms of the density contrast $\chi = \frac{\bar{\rho}|_{z=0}}{\bar{\rho}|_{z=1}}$ via $N_\rho = \ln \chi$.

We solve the above anelastic equations subject to impenetrable, stress-free, and fixed entropy boundary conditions. In particular,

$$w = \frac{\partial u}{\partial z} = \frac{\partial v}{\partial z} = 0 \quad \text{on } z = 0, 1, \quad (11)$$

$$S = \Delta S \quad \text{on } z = 0, \quad S = 0 \quad \text{on } z = 1, \quad (12)$$

where $\Delta S = \bar{s}|_{z=1} = -\frac{1}{\theta} \ln(1 + \theta)$.

TABLE I. Simulation parameters. The first column gives each simulation a name, the letter being the set the simulation belongs to and the number the value of N_ρ in that simulation. We consider four sets of simulations A–D. A and B are from regime (i), weakly rotating, and C and D from regime (ii), rapidly rotating. The second and third columns give the value of Ra and Ta at the bottom boundary, respectively. The fourth column gives the latitude ϕ . Sets A and C have the rotation axis aligned with gravity ($\phi = 90^\circ$), while sets B and D have $\phi = 45^\circ$. The fifth column gives the value of N_ρ ; within each set we consider a range of N_ρ from 0 to 5. The sixth and seventh columns give the value of Ro_c on the bottom and top boundaries, respectively. The final column gives the resolution $n_x \times n_y \times n_z$; here n_i corresponds to the number of spectral modes used in the i direction after 2/3 dealiasing has been applied, that is, 3/2 times n_i is the number of grid points in physical spaces used in the i direction. Note the only difference between simulations B0 and B0* and between B5 and B5* was the state used to initialize each simulation. Simulations B0 and B5* were started from zero velocity and small entropy perturbations (and in particular had no vertically integrated horizontal momentum initially), whereas B0* and B5 were started from states which possessed a nonzero vertically integrated horizontal momentum.

| Name | Ra | Ta | ϕ | N_ρ | $Ro_{c,bot}$ | $Ro_{c,top}$ | $n_x \times n_y \times n_z$ |
|---------|-----------------|-----------------|--------|----------|--------------|--------------|-----------------------------|
| A0 | 4×10^5 | 4×10^4 | 90 | 0 | 3.16 | 3.16 | $128 \times 128 \times 128$ |
| A1 | 4×10^5 | 4×10^4 | 90 | 1 | 3.16 | 4.41 | $192 \times 192 \times 128$ |
| A2 | 4×10^5 | 4×10^4 | 90 | 2 | 3.16 | 6.16 | $192 \times 192 \times 128$ |
| A3 | 4×10^5 | 4×10^4 | 90 | 3 | 3.16 | 8.60 | $192 \times 192 \times 128$ |
| A4 | 4×10^5 | 4×10^4 | 90 | 4 | 3.16 | 12.00 | $256 \times 256 \times 128$ |
| A5 | 4×10^5 | 4×10^4 | 90 | 5 | 3.16 | 16.74 | $256 \times 256 \times 128$ |
| B0, B0* | 4×10^5 | 4×10^4 | 45 | 0 | 3.76 | 3.76 | $128 \times 128 \times 128$ |
| B1 | 4×10^5 | 4×10^4 | 45 | 1 | 3.76 | 5.25 | $192 \times 192 \times 128$ |
| B2 | 4×10^5 | 4×10^4 | 45 | 2 | 3.76 | 7.32 | $192 \times 192 \times 128$ |
| B3 | 4×10^5 | 4×10^4 | 45 | 3 | 3.76 | 10.22 | $192 \times 192 \times 128$ |
| B4 | 4×10^5 | 4×10^4 | 45 | 4 | 3.76 | 14.27 | $256 \times 256 \times 128$ |
| B5, B5* | 4×10^5 | 4×10^4 | 45 | 5 | 3.76 | 19.91 | $256 \times 256 \times 128$ |
| C0 | 1×10^7 | 2×10^8 | 90 | 0 | 0.22 | 0.22 | $384 \times 384 \times 128$ |
| C1 | 1×10^7 | 2×10^8 | 90 | 1 | 0.22 | 0.31 | $384 \times 384 \times 128$ |
| C2 | 1×10^7 | 2×10^8 | 90 | 2 | 0.22 | 0.44 | $512 \times 512 \times 128$ |
| C3 | 1×10^7 | 2×10^8 | 90 | 3 | 0.22 | 0.61 | $512 \times 512 \times 128$ |
| C4 | 1×10^7 | 2×10^8 | 90 | 4 | 0.22 | 0.85 | $512 \times 512 \times 192$ |
| C5 | 1×10^7 | 2×10^8 | 90 | 5 | 0.22 | 1.18 | $512 \times 512 \times 192$ |
| D0 | 1×10^7 | 2×10^8 | 45 | 0 | 0.27 | 0.27 | $384 \times 384 \times 128$ |
| D1 | 1×10^7 | 2×10^8 | 45 | 1 | 0.27 | 0.37 | $384 \times 384 \times 128$ |
| D2 | 1×10^7 | 2×10^8 | 45 | 2 | 0.27 | 0.52 | $512 \times 512 \times 128$ |
| D3 | 1×10^7 | 2×10^8 | 45 | 3 | 0.27 | 0.72 | $512 \times 512 \times 128$ |
| D4 | 1×10^7 | 2×10^8 | 45 | 4 | 0.27 | 1.01 | $512 \times 512 \times 192$ |
| D5 | 1×10^7 | 2×10^8 | 45 | 5 | 0.27 | 1.41 | $512 \times 512 \times 192$ |

Throughout this paper we consider a domain of size $2\pi \times 2\pi \times 1$ (in dimensionless units) with periodic boundaries in the horizontal directions. We solve the system described above, with a pseudospectral numerical code written in DEDALUS [58,59]. We use a Crank-Nicolson, Adams-Bashforth second-order, semi-implicit time-stepping scheme. The time step is allowed to vary according to a standard Courant-Friedrichs-Lewy criterion. The spatial resolutions used are quoted in Table I (note that these values give the number of spectral modes after dealiasing; the number of grid point used can be found by multiplying this number by 3/2).

Derived quantities

In addition to the input dimensionless quantities given in (8), it is useful to define some diagnostic quantities that are derived from simulation output in order to help characterize the system. The

Rossby number is a measure of the strength of inertia relative to Coriolis forces and we calculate it as a function of depth from our simulations using the definition

$$\text{Ro}(z) = \left\langle \frac{\sqrt{|\mathbf{u} \cdot \nabla \mathbf{u}|^2}}{\sqrt{|\boldsymbol{\Omega} \times \mathbf{u}|^2}} \right\rangle_{x,y}, \quad (13)$$

where angular brackets $\langle \cdot \rangle_{x,y}$ denote an average over horizontal planes. Since this quantity is unknown before the simulation has run, the so-called convective Rossby number $\text{Ro}_c = \sqrt{\text{Ra}/\text{TaPr} \sin \phi}$ (for $\phi \neq 0$) is sometimes used as an *a priori* measure of the relative strength of inertia to Coriolis force. Note that, for $N_\rho = 0$ ($\theta = 0$), Ro_c is constant across the layer, but for $N_\rho \neq 0$ ($\theta \neq 0$), $\text{Ro}_c \propto (1 + \theta z)^{-1/2}$ and so increases with z . We will address the question of how good a proxy Ro_c is for Ro in our simulations in Sec. III A.

To quantify the effect of stratification on convective heat transport, we use the Nusselt number, which we define as the ratio of the total heat flux to the conductive heat flux of the base state, i.e.,

$$\text{Nu} = \frac{\left(\frac{\partial S}{\partial z}\right)}{\left(\frac{dS}{dz}\right)} = -(1 + \theta z) \frac{\partial S}{\partial z}. \quad (14)$$

This gives Nu at the bottom of the layer as $\text{Nu}|_{z=0} = -\frac{\partial S}{\partial z}|_{z=0}$ and Nu at the top as $\text{Nu}|_{z=1} = -(1 + \theta) \frac{\partial S}{\partial z}|_{z=1}$; we expect these to be equal in a steady state.

III. RESULTS

We consider a series of numerical simulations using the setup described in Sec. II. The onset of compressible convection in a local Cartesian geometry assuming the anelastic approximation varies depending on the precise form of the anelastic approximation utilized [60–62]. The linear problem for the particular formalism described in Sec. II was studied by Mizerski and Tobias [55] for the case gravity and rotation aligned and extended by Currie and Tobias [30] to consider the case of tilted rotation. In this paper we focus on the nonlinear regime and discuss the role of stratification in modifying the dynamics of convection in two cases: (i) a weakly rotating regime, where the large-scale flow takes the form of a vertical shear, and (ii) a rapidly rotating regime, where it has the character of a large-scale vortex. Within each regime, we consider tilted and untilted cases for a range of stratifications spanning $N_\rho = 0$ (Boussinesq) to $N_\rho = 5$. Within each subset of simulations, we fix Ro_c at the bottom of the domain. We note that the Reynolds number of the two regimes is not comparable. The cases are selected to be at different convective Rossby numbers (at the bottom of the computational domain), and this leads to different dynamics in particular to the response of the convection to rotation. The dependence of Reynolds number on Rayleigh number is known to be a function of rotation rate [63], and so any attempt to fix the Reynolds number across parameter regimes *a priori* is difficult. Furthermore, the Reynolds number will turn out to be a strong function of depth for stratified convection. A summary of the input parameters used in our simulations is given in Table I. Each subset of simulations is given a name (A–D) for ease of reference and each simulation within each subset is given a number to reflect the value of N_ρ (see the first column of Table I).

A. Solution regimes

Regimes (i) and (ii) lead to flows with very different morphologies, as perhaps expected. Typical snapshots of the vertical velocity from each regime are shown in Fig. 3. Figures 3(a) and 3(b) show the snapshots from a weakly rotating case for a Boussinesq simulation and for a simulation with $N_\rho = 5$, respectively. In both cases the rotation is aligned vertically and the convection cells show alignment with the rotation axis but the horizontal length scale of the cells is broad. By contrast, Figs. 3(c) and 3(d) show more rapidly rotating cases for a Boussinesq case and a case with $N_\rho = 5$, respectively. Again, in both cases the rotation is aligned vertically. In these cases, thin convection

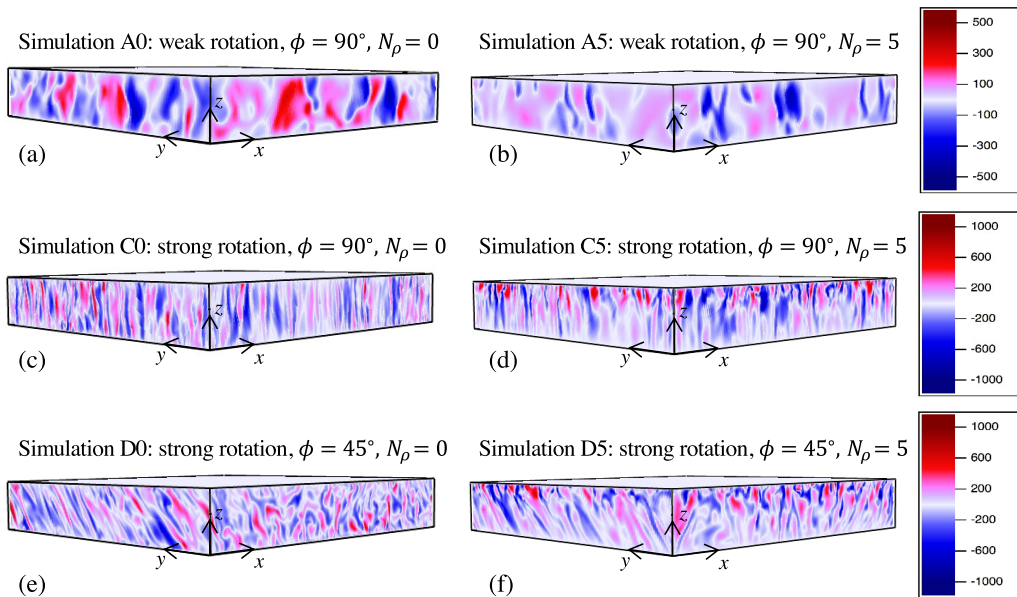


FIG. 3. Snapshots of the vertical velocity w for six different simulations as defined in Table I: (a) $Ro_{c,bot} = 3.16$, $\phi = 90^\circ$, and $N_\rho = 0$ (simulation A0); (b) $Ro_{c,bot} = 3.16$, $\phi = 90^\circ$, and $N_\rho = 5$ (simulation A5); (c) $Ro_{c,bot} = 0.22$, $\phi = 90^\circ$, and $N_\rho = 0$ (simulation C0); (d) $Ro_{c,bot} = 0.22$, $\phi = 90^\circ$, and $N_\rho = 5$ (simulation C5); (e) $Ro_{c,bot} = 0.27$, $\phi = 45^\circ$, and $N_\rho = 0$ (simulation D0); and (f) $Ro_{c,bot} = 0.27$, $\phi = 45^\circ$, and $N_\rho = 5$ (simulation D5). Rotation causes the convection cells to align with the rotation axis, but stratification disrupts the independence along this direction.

cells are seen that align with the rotation axis, as might be expected from the Taylor-Proudman theorem. We note that the Reynolds number for simulation set C is larger than in simulation set A and so the role of turbulence is stronger. However, a more significant effect is that the convective Rossby number, which gives a measure of the strength of advection relative to rotation, is much smaller (at the bottom of the domain) in set C, and this is reflected in the dynamics. In the Boussinesq case, these cells extend relatively uniformly across the height of the domain, whereas in the stratified case, the vertical velocity is larger at the top of the domain where the density is lower (this effect will be studied in more detail in Sec. III B). This effect of stratification is more evident in the rapidly rotating case than in the weakly rotating one; however, even in the weakly rotating case, there is still an asymmetry in the layer.

In Figs. 3(e) and 3(f) the parameters are the same as in Figs. 3(c) and 3(d), except now the rotation vector is tilted to 45° . In this case, the convection cells are tilted in the y - z plane to align approximately with the direction of the rotation vector, again a consequence of the strong rotation. The width of the convection cells in the bottom row are perhaps slightly larger than in the second row; this is likely to be a consequence of the reduced vertical component of rotation. Again the effect of stratification is evident in Fig. 3(f), where the flow velocity is stronger near the top of the layer.

The time taken for some of the simulations to reach a statistically steady state from a small random initial perturbation can be long. In particular, in the rapidly rotating cases [regime (ii)], it can take several diffusion times for the kinetic energy to reach a saturated state. The likely reason for this is that in the rapidly rotating cases, a large-scale structure that evolves on the viscous timescale emerges from the convection. Similar structures have been observed in the work of [43,64–68] and will be discussed in more detail in Sec. III B. Therefore, for computational convenience, we ran some fiducial cases starting from rest and others starting from saturated states of previous runs. In

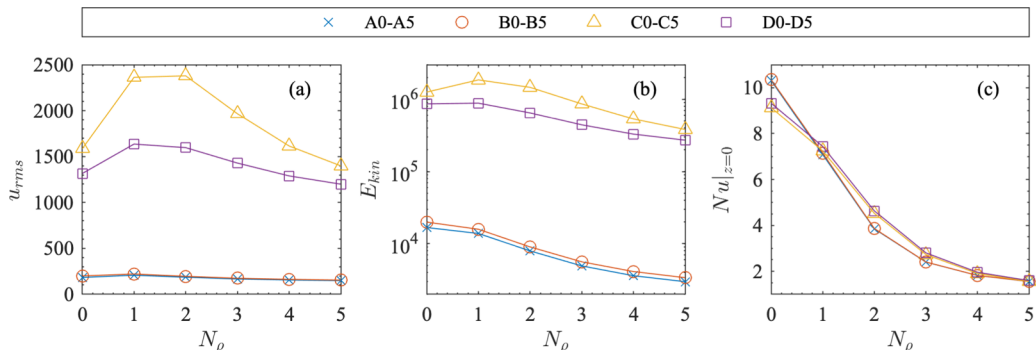


FIG. 4. Plot of (a) u_{rms} , (b) E_{kin} , and (c) Nu as a function of N_ρ for simulations in each of the regimes: A (blue crosses), B (orange circles), C (yellow triangles), and D (purple squares).

contrast, the weakly rotating cases evolve to a statistically steady state well within a thermal or viscous diffusion time.

In Fig. 4 we show time-averaged quantities where the temporal averages are taken over a time interval in which the solution is in a saturated state. We note that for each set of parameter values it may be possible that multiple states can be found (see, e.g., [69]) but we do not investigate this further here. Figure 4(a) shows the time average of u_{rms} for simulations in each of the regimes A–D. Here $u_{\text{rms}} = \sqrt{\langle u^2 + v^2 + w^2 \rangle}$, where the angular brackets denote a volume average. For all four regimes, the general trend is that as N_ρ is increased from zero, u_{rms} first increases, but then as N_ρ is increased further, u_{rms} decreases. This could be a result of competing effects: (i) As N_ρ is increased, the average density is decreased, which we would expect might lead to faster velocities, but (ii) Ra is not constant across the domain and is proportional to $(1 + \theta z)^{m-1}$ [see Fig. 2(a)] and so the fluid becomes less supercritical at higher depths in the layer as N_ρ is increased; this we might expect to lead to slower velocities. (iii) The Prandtl number Pr is small at the top of the layer; low- Pr flows are known to favor flywheel convection where energy is transferred to kinetic energy via the dominance of the inertial terms. For small- Pr flows heat transport is known to be inefficient [70–72]; for example, Clever and Busse [71] found convective heat transport to be relatively independent of Pr for Ra larger than a critical value and $0.001 \leq Pr \leq 0.71$.

The corresponding kinetic energies for simulations in each of the regimes A–D are shown in Fig. 4(b). This measure is affected by the density of the fluid in addition to the fluid velocities and is defined as $E_{\text{kin}} = \langle \bar{\rho}(u^2 + v^2 + w^2) \rangle / 2$. For the high-Rossby-number cases, E_{kin} is a monotonically decreasing function of N_ρ ; while the average velocity increases between $N_\rho = 0$ and $N_\rho = 1$, the decrease in the mean density is a more significant effect, leading to a smaller kinetic energy. By contrast, in the small-Rossby-number cases, the behavior of E_{kin} has a similar trend to that of u_{rms} .

To determine how the stratification affects the convective heat transport, we have calculated the Nusselt number [defined in (14)] for each of our simulations [see Fig. 4(c)]. We see that for all cases here (weakly and rapidly rotating) increasing N_ρ leads to less efficient heat transport (smaller Nu). This is consistent with the numerical and analytical results of Mizerski and Tobias [55]. Since here we fix Ra at the bottom of the domain and the critical Rayleigh number is an increasing function of N_ρ , the supercriticality of the convection is decreased as N_ρ is increased. This should correspond to a decrease in Nu with N_ρ and so in some sense the behavior of Nu in Fig. 4(c) is not a surprise. However, if the change in supercriticality were the only effect we would expect E_{kin} and u_{rms} to decrease monotonically with N_ρ but, as discussed above, this is not the case. This suggests that the influence of stratification on heat transport is more complicated.

We find that Nu for all the simulations examined here reaches a statistically steady state well within a thermal diffusion time [even in regime (ii) where the kinetic energy may not reach a statistically steady state for several diffusion times]. This implies that the heat flux does not change

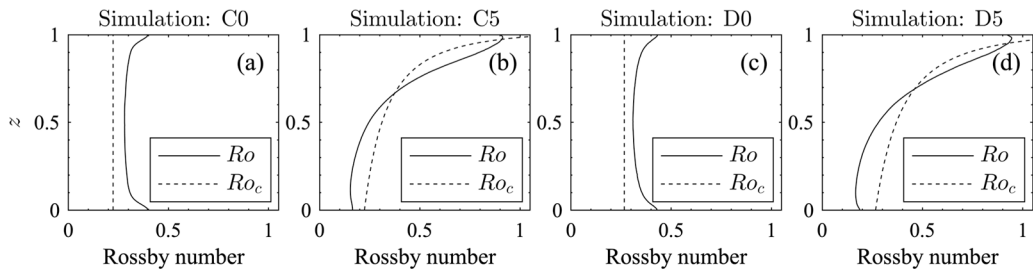


FIG. 5. Rossby number as a function of depth for cases with $\phi = 90^\circ$ and (a) $N_\rho = 0$ (simulation C0) and (b) $N_\rho = 5$ (simulation C5) and for cases with $\phi = 45^\circ$ and (c) $N_\rho = 0$ (simulation D0) and (d) $N_\rho = 5$ (simulation D5). In each case a Rossby number calculated from input parameters (Ro_c) and a Rossby number calculated from outputs of the simulation (Ro) are included.

much as the large-scale convective structures (investigated further in Sec. III B) continue to form over a slow timescale.

Figure 5 shows Ro [as defined in (13)] for rapidly rotating simulations with $N_\rho = 0$ (Boussinesq) and $N_\rho = 5$. In Figs. 5(a) and 5(b), $\phi = 90^\circ$ and the rotation vector is aligned with gravity and in Figs. 5(c) and 5(d), $\phi = 45^\circ$. In the Boussinesq cases, Ro is roughly constant across the domain and is in the regime we expect rotation to dominate ($Ro \ll 1$). For $N_\rho = 5$, Ro increases significantly from the bottom to the top of the domain, suggesting a reduction in the influence of rotation as we move higher in the layer. We have also plotted Ro_c (which has the advantage that it can be calculated before the simulation started) and it seems (at least for these cases) to perform well in describing the effect of rotation relative to inertia over the depth of the domain.

B. Large-scale flows

1. Regime (i): Weakly rotating

As has been shown in previous studies (e.g., [25,30] and references therein), convection is able to generate coherent mean (i.e., horizontally averaged) flows when the rotation vector is not aligned with gravity. For example, in Figs. 6(a) and 6(b), systematic $\langle u \rangle_{x,y}$ and $\langle v \rangle_{x,y}$ are generated in time. In these cases, the system is Boussinesq and as expected there is a symmetry about $z = 0.5$, as indicated by the dotted horizontal lines; above $z = 0.5$, u is predominantly negative and v positive, while below $z = 0.5$, u is predominantly positive and v negative. Keeping all other parameters fixed and increasing N_ρ to 5 leads to the mean flows shown in Figs. 6(c) and 6(d). While still present, the flows are now less systematic and more oscillatory; for example, u oscillates between positive and negative flow across most of the layer depth but with a preference for negative flow in a time-averaged sense. At each time, the magnitude of the flows is similar to the Boussinesq case but the oscillations result in a smaller time-averaged flow. We note that these $N_\rho = 5$ flows were obtained from a simulation which started from an existing solution that has a nonzero vertically integrated horizontal momentum, and therefore the vertically integrated horizontal momentum is not necessarily zero at each time. This can be seen if we first consider the horizontally averaged, horizontal momentum equations

$$\frac{\partial}{\partial t}(\bar{\rho}u) + \frac{\partial}{\partial z}(\bar{\rho}uw) = \text{Ta}^{1/2}\text{Pr} \sin \phi \bar{\rho}v + \text{Pr} \frac{\partial}{\partial z} \left(\bar{\rho} \frac{\partial \bar{u}}{\partial z} \right), \quad (15)$$

$$\frac{\partial}{\partial t}(\bar{\rho}v) + \frac{\partial}{\partial z}(\bar{\rho}vw) = -\text{Ta}^{1/2}\text{Pr} \sin \phi \bar{\rho}u + \text{Pr} \frac{\partial}{\partial z} \left(\bar{\rho} \frac{\partial \bar{v}}{\partial z} \right). \quad (16)$$

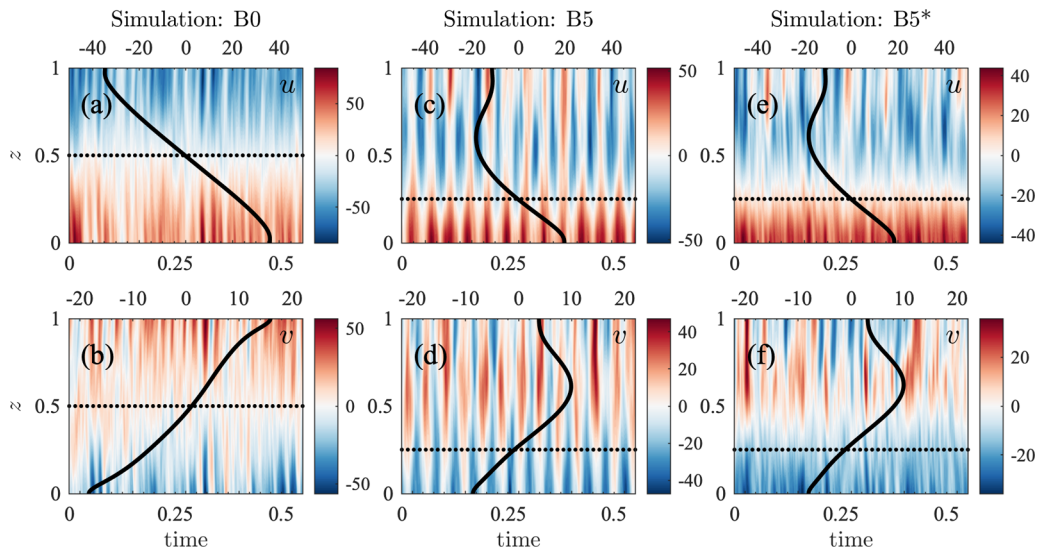


FIG. 6. Horizontally averaged (mean) horizontal flow component (a), (c), and (e) $\langle u \rangle_{x,y}$ and (b), (d), and (f) $\langle v \rangle_{x,y}$ as a function of time and z (contours, colorbar) and time-averaged mean flow (black line, top axis) for simulations (a) and (b) B0, (c) and (d) B5, and (e) and (f) B5*. Note that the only difference between simulations B5 and B5* is the state from which each simulation was initialized. The horizontal dotted lines denote the depth at which the center of mass lies.

If we then integrate these over z , we find equations for the vertically integrated horizontal momentum

$$\frac{\partial}{\partial t} \left(\int \bar{\rho} \bar{u} dz \right) = \text{Ta}^{1/2} \text{Pr} \sin \phi \int \bar{\rho} \bar{v} dz, \quad (17)$$

$$\frac{\partial}{\partial t} \left(\int \bar{\rho} \bar{v} dz \right) = -\text{Ta}^{1/2} \text{Pr} \sin \phi \int \bar{\rho} \bar{u} dz, \quad (18)$$

where we have made use of the velocity boundary conditions in (11). It follows from (17) and (18) that if $\int \bar{\rho} \bar{u} dz$ and $\int \bar{\rho} \bar{v} dz$ are zero initially, they must remain so for all time, but not otherwise. By differentiating (17) and substituting into (18) (and vice versa) one can see that (when they are nonzero initially) the components of vertically integrated horizontal momentum are governed by wave equations. Figures 6(e) and 6(f) show the equivalent case to Figs. 6(c) and 6(d) but starting from an initial condition with zero velocity. Unlike in Figs. 6(c) and 6(d) where there is significant transfer between \bar{u} and \bar{v} owing to the rotation, here there is no such transfer. The exchange between \bar{u} and \bar{v} in Figs. 6(c) and 6(d) results in a spiraling of the mean flow that is not observed in the case shown in Figs. 6(e) and 6(f) (see the Supplemental Material [73] for corresponding movies of simulations B5 and B5* which show most clearly the spiraling of the flow in simulation B5 but not in B5*). We remark further that if we initialize a Boussinesq simulation with an initial condition that has a nonzero vertically integrated horizontal momentum (simulation B0*), then that case will also possess a non trivial vertically integrated horizontal momentum at later times [as governed by the wave equation resulting from Eqs. (17) and (18)]. However, even with a nonzero vertically integrated momentum, the mean flow in this Boussinesq case does not exhibit spiraling (see the Supplemental Material [73] for movies of the mean flows in simulations B0 and B0*). In summary, the stratification appears to introduce a symmetry breaking that leads to a spiraling mean flow (in those cases which initially have some vertically integrated horizontal momentum) that is not seen in the Boussinesq cases. Note that we find bulk properties such as those displayed in Fig. 4 to be the

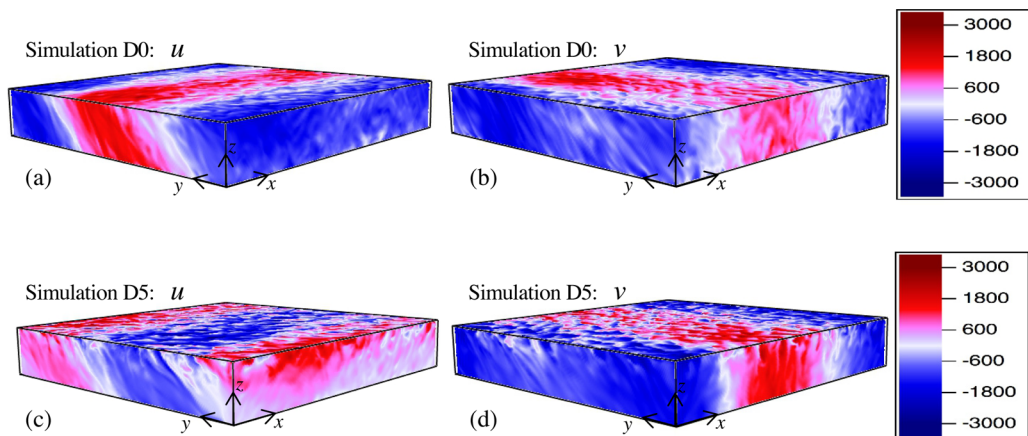


FIG. 7. Snapshots of the horizontal velocities (a) and (c) u and (b) and (d) v for two different simulations: (a) and (b) simulation D0 ($N_\rho = 0$) and (c) and (d) simulation D5 ($N_\rho = 5$).

same in both the two $N_\rho = 5$ cases with different initial conditions and the two Boussinesq cases with different initial conditions.

Regardless of the initial condition, stratification introduces an asymmetry in the layer; the depth in the layer at which $\langle u \rangle_{x,y}$ and $\langle v \rangle_{x,y}$ cross zero occurs approximately around the depth at which the center of mass lies (this is marked with the horizontal dotted line in the plots). This transition depth was also suggested in the fully compressible studies of Brummell *et al.* [46] and is a consequence of momentum conservation and stress-free boundary conditions. The self-consistently generated mean flow that is produced in this regime has strong vertical shear, which may have important consequences for dynamos and the viability of such flows to drive a large-scale dynamo are discussed further in Sec. III C.

2. Regime (ii): Rapidly rotating

In regime (ii) (simulation subsets C and D), Ro_c is much smaller than in regime (i). In these cases there are no systematic mean flows like those discussed in the preceding section but instead large-scale coherent jets form which often correspond to a large-scale vortex. These structures have been investigated in a number of different systems: in compressible convection by Mantere *et al.* [64] and Chan and Mayr [65], in an asymptotic model with polar rotation by Rubio *et al.* [66], and in a Boussinesq model by Favier *et al.* [67] and Guervilly *et al.* [68]. More recently, they were observed at an arbitrary latitude by Novi *et al.* [43] and Currie *et al.* [74]. A classic example of these flows is given in Fig. 7, where the left-hand (right-hand) column shows u (v) for a Boussinesq case [Figs. 7(a) and 7(b)] and a case with $N_\rho = 5$ [Figs. 7(c) and 7(d)]. In both cases, u (v) varies very little along the x (y) direction and contains one wavelength in y (x); it is clear that averaging over y (x) will lead to the positive and negative jets canceling out and therefore no systematic mean flows exist in these cases.

Figure 3 suggested that while in the Boussinesq case the convective cell structures are largely independent of the direction of the rotation axis, at strong stratification there is variation along Ω . This effect can also be seen to some extent in the stratified snapshots of u and v in Figs. 7(c) and 7(d), respectively. This reduction in the extent to which the Taylor-Proudman constraint is satisfied as stratification is increased is exhibited more clearly in Fig. 8, where vertical slices of the flow and the corresponding perturbations that remain after an average along the rotation axis has been subtracted are shown. In the Boussinesq cases in Figs. 7(a) and 7(b), the departures from a perfect Taylor-Proudman state are fairly uniform across the depth of the layer. By contrast, for $N_\rho = 5$, the

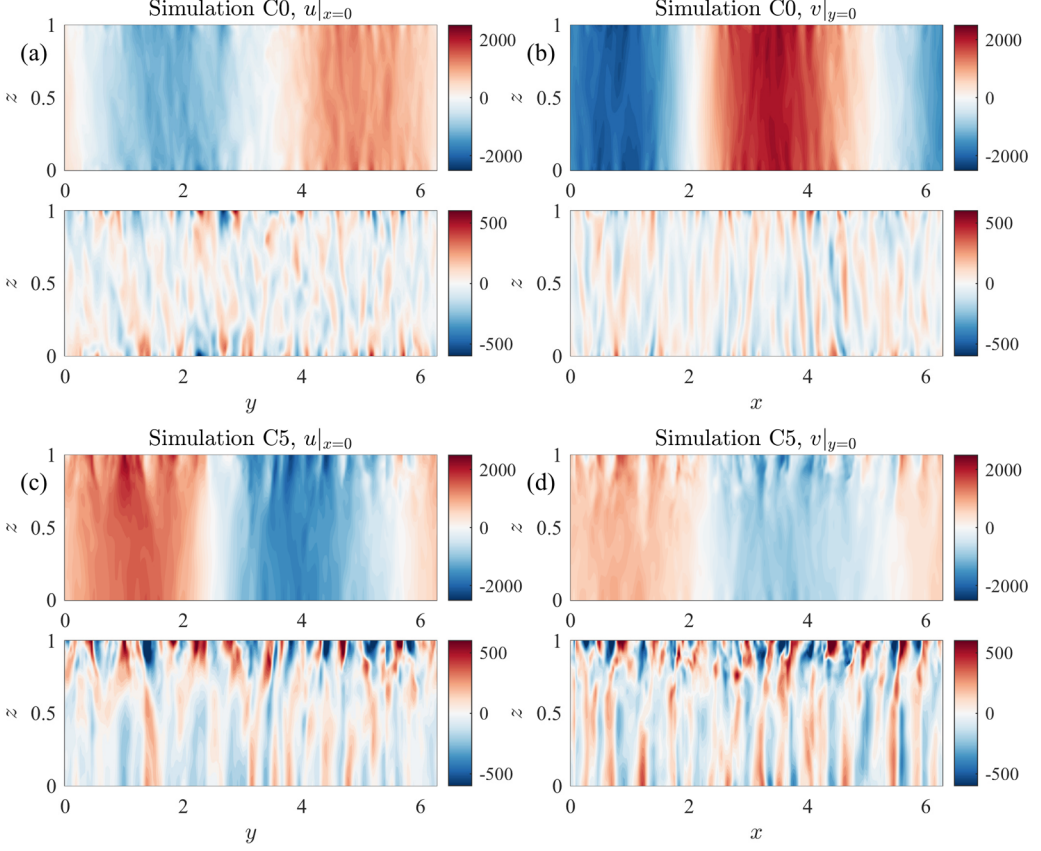


FIG. 8. Slices of the horizontal velocities. For (a) and (c) u the slices are taken at $x = 0$ and (b) and (d) v the slices are taken at $y = 0$. In (a) and (b), $N_\rho = 0$ (simulation C0) and in (c) and (d), $N_\rho = 5$ (simulation C5). Within each figure, the top panel gives the slice of the velocity component in that plane and the bottom panel gives the perturbations that remain when the average along the rotation axis is subtracted.

departures are much larger at the top of the domain. In addition, the magnitude of the perturbations are relatively larger in the strongly stratified case.

Mathematically speaking, the departures from Taylor-Proudman can be seen by the extra terms present in the vorticity equation. The x , y , and Ω (i.e., along the direction of the rotation axis) components of the vorticity equation [formed by taking the curl of Eq. (3)] are

$$\begin{aligned} & \frac{\partial \omega_x}{\partial t} + (\mathbf{u} \cdot \nabla) \omega_x - (\boldsymbol{\omega} \cdot \nabla) u - \frac{m\theta w}{1 + \theta z} \omega_x \\ & = \text{Ta}^{1/2} \text{Pr} (\boldsymbol{\Omega} \cdot \nabla) u + \text{Ra Pr} \frac{\partial S}{\partial y} + \text{Pr} \nabla^2 \omega_x + \frac{\text{Pr} m \theta}{1 + \theta z} \left(\frac{\partial \omega_x}{\partial z} + \frac{(1 + 2m)\theta}{3(1 + \theta z)} \frac{\partial w}{\partial y} \right), \end{aligned} \quad (19)$$

$$\begin{aligned} & \frac{\partial \omega_y}{\partial t} + (\mathbf{u} \cdot \nabla) \omega_y - (\boldsymbol{\omega} \cdot \nabla) v - \frac{m\theta w}{1 + \theta z} \omega_y \\ & = \text{Ta}^{1/2} \text{Pr} \cos \phi \frac{m\theta w}{1 + \theta z} + \text{Ta}^{1/2} \text{Pr} (\boldsymbol{\Omega} \cdot \nabla) v - \text{Ra Pr} \frac{\partial s}{\partial x} \\ & + \text{Pr} \nabla^2 \omega_y + \frac{\text{Pr} m \theta}{1 + \theta z} \left(\frac{\partial \omega_y}{\partial z} - \frac{(1 + 2m)\theta}{3(1 + \theta z)} \frac{\partial w}{\partial x} \right), \end{aligned} \quad (20)$$

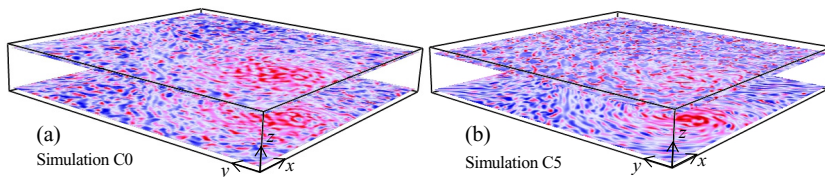


FIG. 9. Snapshots of the vertical vorticity for (a) simulation C0 ($N_\rho = 0$) and (b) simulation C5 ($N_\rho = 5$). In (a) a large-scale vortex is clearly seen to extend across the depth of the domain, while in (b) the vortex is only seen at the bottom of the domain.

$$\begin{aligned}
 & \frac{\partial \omega_\Omega}{\partial t} + (\mathbf{u} \cdot \nabla) \omega_\Omega - (\boldsymbol{\omega} \cdot \nabla) u_\Omega - \frac{m\theta w}{1 + \theta z} \omega_\Omega \\
 &= \text{Ta}^{1/2} \text{Pr} \frac{m\theta w}{1 + \theta z} + \text{Ta}^{1/2} \text{Pr} (\boldsymbol{\Omega} \cdot \nabla) u_\Omega - \text{Ra} \text{Pr} \cos \phi \frac{\partial s}{\partial x} \\
 &+ \text{Pr} \nabla^2 \omega_\Omega + \frac{\text{Pr} m \theta}{1 + \theta z} \left(\frac{\partial \omega_\Omega}{\partial z} - \frac{(1 + 2m)\theta}{3(1 + \theta z)} \cos \phi \frac{\partial w}{\partial x} \right), \tag{21}
 \end{aligned}$$

where $\boldsymbol{\omega} = \nabla \times \mathbf{u} = (\omega_x, \omega_y, \omega_z)$ is the vorticity and $\omega_\Omega = \boldsymbol{\omega} \cdot \boldsymbol{\Omega}$ and $u_\Omega = \mathbf{u} \cdot \boldsymbol{\Omega}$ are the components of $\boldsymbol{\omega}$ and \mathbf{u} along $\boldsymbol{\Omega}$, respectively.

If Ro is small, we expect $\text{Ta}^{1/2} \text{Pr} (\boldsymbol{\Omega} \cdot \nabla) u \sim 0$ to be the dominant balance in (19) and so variations in u should be independent along $\boldsymbol{\Omega}$ irrespective of N_ρ . In (20) a departure from $\text{Ta}^{1/2} \text{Pr} (\boldsymbol{\Omega} \cdot \nabla) v \sim 0$ is introduced if $\phi \neq \frac{\pi}{2}$ and $\theta \neq 0$ (and is given by $\text{Ta}^{1/2} \text{Pr} \cos \phi \frac{m\theta w}{1 + \theta z}$). Similarly, in (21), a departure from $\text{Ta}^{1/2} \text{Pr} (\boldsymbol{\Omega} \cdot \nabla) u_\Omega \sim 0$ is introduced if $\theta \neq 0$ (given by $\text{Ta}^{1/2} \text{Pr} \frac{m\theta w}{1 + \theta z}$). This suggests that departures from a perfect Taylor-Proudman state in u are a result of the nonlinear inertial terms contributing significantly. In fact, if we consider the depth-dependent Ro for the cases shown in Fig. 8 [see Figs. 5(a) and 5(b)], then Ro is order 1 at the top of the domain, which suggests that the inertia terms are not completely dominated by the Coriolis force. This effect may also be present in causing departures from a Taylor-Proudman state in v and w . Moreover, we would expect that in a regime where Ro is small across the whole depth, departures from a Taylor-Proudman state can still be introduced by the additional terms in (20) and (21) introduced by stratification.

As mentioned before, the large-scale structures in the velocity components may correspond to a large-scale vortex as seen in several previous studies. To examine these structures, the component of vorticity along the rotation axis is shown in Fig. 9. In the Boussinesq case, a concentrated region of positive vorticity can be seen in the layers near the top and bottom of the layer. This is indicative of a vortex that extends across the whole depth, in line with what has been seen in previous studies. However, in the strongly stratified case, the vortex can clearly be seen near the bottom of the layer but not near the top of the domain. We note that the vortex appears to maintain the same sign of vorticity as the stratification is changed.

The prevalence of an inverse cascade (leading to a vortex) can be examined further by considering a shell-to-shell energy transfer analysis [67,75]. We focus on the transfer function $T(Q, K, z)$, which represents the energy transfer from shell Q to shell K at a height z . In this context, a shell K is defined in wave-number space as those wave numbers that satisfy $K < k_h \leq K + 1$, where $k_h = \sqrt{k_x^2 + k_y^2}$ is the horizontal wave number (k_x and k_y are the wave numbers in the x and y directions, respectively). We then define a filtered field \mathbf{u}_K such that

$$\mathbf{u}_K(x, y, z) = \sum_{K < k_h \leq K+1} \hat{\mathbf{u}}(k_x, k_y, z) e^{ik_x x + ik_y y}, \tag{22}$$

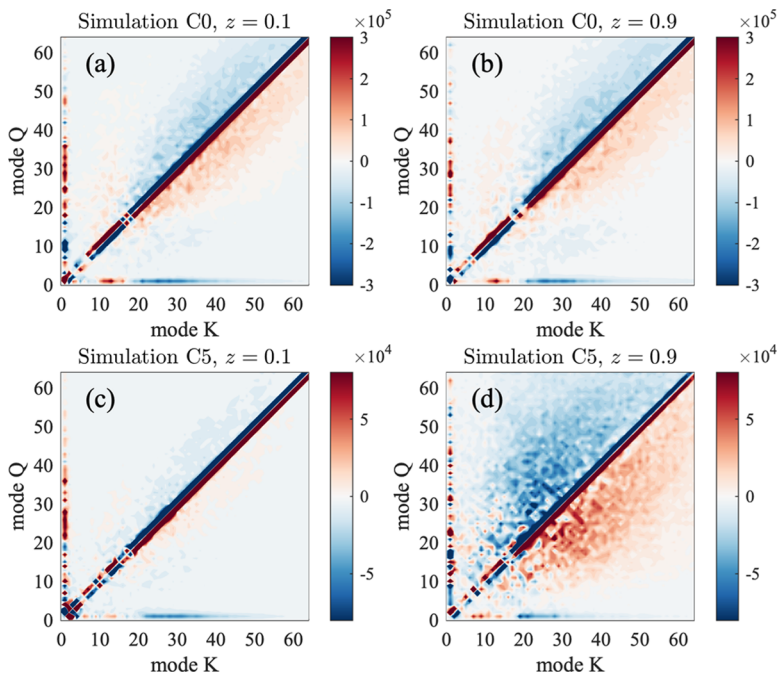


FIG. 10. Slices at a fixed depth of time-averaged transfer functions $T(Q, K, z)$ for shells with $0 < Q, K < 64$ at (a) $z = 0.1$ and (b) $z = 0.9$ for simulation C0 ($N_\rho = 0$) and (c) $z = 0.1$ and (d) $z = 0.9$ for simulation C5 ($N_\rho = 5$). The function is positive when energy is extracted from shell Q and given to shell K .

and then $T(Q, K, z)$ is given (for all z) by

$$T(Q, K, z) = - \int \bar{\rho} \mathbf{u}_K \cdot [(\mathbf{u} \cdot \nabla) \mathbf{u}_Q] dx dy. \quad (23)$$

The transfer function $T(Q, K, z)$ can be interpreted as follows: If $T(Q, K, z)$ is positive, then a positive amount of energy is extracted from shell Q and given to shell K . Note that if an average is taken over all depths z then $\bar{T}(Q, K) = -\bar{T}(K, Q)$, where $\bar{T} = \int T dz$, but this does not have to hold at each z .

In Fig. 10 we plot $T(Q, K, z = 0.1)$ and $T(Q, K, z = 0.9)$ averaged over several snapshots for $N_\rho = 0$ [Figs. 10(a) and 10(b)] and for $N_\rho = 5$ [Figs. 10(c) and 10(d)]. Here we see that for $N_\rho = 0$ the results are entirely consistent with those of Favier *et al.* [67]; the large-scale structure is fed by nonlocal energy transfer into large-scale modes. As the structure is baroclinic, the transfer is the same at $z = 0.1$ and $z = 0.9$. In contrast, for the $N_\rho = 5$ stratified case, while the nonlocal transfer is still effective towards the bottom of the domain (in the low-Ro region), it is significantly disrupted at $z = 0.9$. Hence relatively less energy is channeled to the coherent structure.

As with the reduction in the Taylor-Proudman constraint that occurs near the top of the domain, the nonexistence of a vortex there can perhaps be explained by considering the Rossby number as a function of depth. The Rossby number Ro was shown for these cases in Figs. 5(a) and 5(b) and as discussed there it is much larger at the top of the domain than at the bottom, when $N_\rho = 5$. This implies that the rotational dominance is greatly reduced at the top of the domain.

C. Effect of stratification on net helicity

From a dynamo perspective, we are interested in if these flows can generate a large-scale, systematic, magnetic field. In this case, lack of reflectional symmetry often as manifested by kinetic

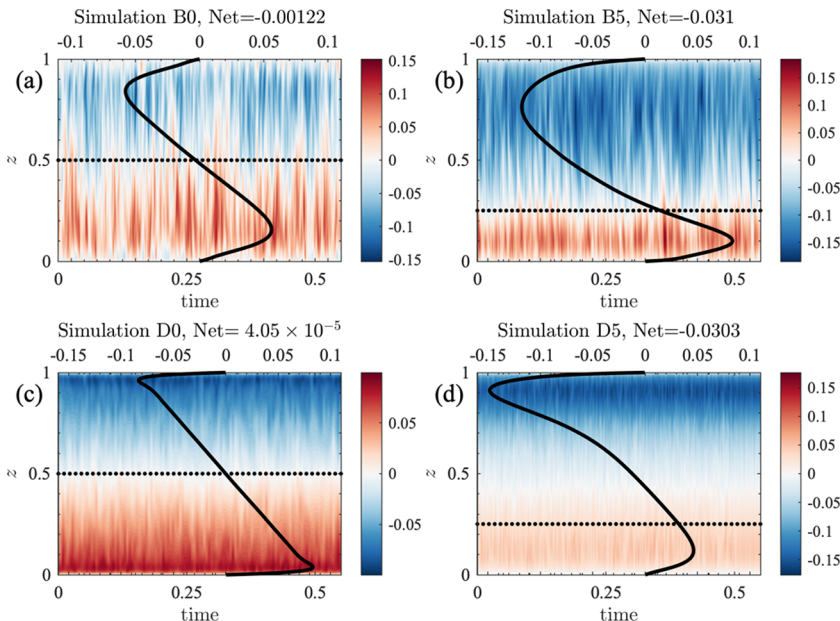


FIG. 11. Relative helicity in the perturbations (i.e., after the horizontal mean flow has been removed) as a function of z and time (contours, colorbar) for (a) simulation B0, (b) simulation B5, (c) simulation D0, and (d) simulation D5. The time-averaged relative helicity is given by the over-plotted black lines (top axes). The net helicity (time and vertically averaged value) for each case is displayed at the top of each panel. The horizontal dotted lines denote the depth at which the center of mass lies.

helicity is believed to be an important quantity [76]. The relative helicity is given by

$$h(z) = \left\langle \frac{\langle \mathbf{u}' \cdot \boldsymbol{\omega}' \rangle_{x,y}}{\langle \mathbf{u}'^2 \rangle_{x,y}^{1/2} \langle \boldsymbol{\omega}'^2 \rangle_{x,y}^{1/2}} \right\rangle_t, \quad (24)$$

where $\boldsymbol{\omega}' = \nabla \times \mathbf{u}'$ is the vorticity, $\langle \cdot \rangle_t$ denotes an average over t , and $\mathbf{u}' = \mathbf{u} - \langle \mathbf{u} \rangle_{x,y}$ is the fluctuation of \mathbf{u} about its mean state $\langle \mathbf{u} \rangle_{x,y}$. Since we are really interested in the helicity of the turbulent eddies and not the large-scale component of the flow, we use \mathbf{u}' in the calculation of h .

In the Boussinesq cases, we expect an average of $h(z)$ over z to lead to zero net helicity and this is what is essentially seen in Figs. 11(a) and 11(c) where the negative helicity in the top half of the layer cancels with the positive helicity in the bottom half. As we have seen, stratification introduces an asymmetry; this results in the flows possessing a nonzero net helicity, when averaged over the whole domain [see Figs. 11(b) and 11(d)]. It has been shown by Cattaneo and Tobias [77], Nigro *et al.* [78], and Pongkitiwanchakul *et al.* [79] that a large-scale magnetic field can be generated even for turbulent flows if the product of the shear and helicity is large enough. However, for the cases studied here, even though we find that the net helicity increases approximately linearly with N_ρ , it is small even for $N_\rho = 5$ and it remains to be seen if this is enough to generate large-scale dynamo waves. This might depend on the location of strongest shear.

IV. DISCUSSION AND CONCLUSIONS

In this paper we have examined the effect of stratification on two key regimes of rotating anelastic convection, with both a vertical and tilted (to the direction of gravity) rotation vector. These regimes correspond to (i) weakly rotating ($\text{Ro} > 1$) and (ii) rapidly rotating ($\text{Ro} \ll 1$) flows. It is known that density stratification introduces an asymmetry that leads to significantly faster velocities at the

top of the domain. Moreover, the variation in Ra and Pr in strongly stratified cases for the setup considered here means the convection may behave quite differently at different depths, thus having a significant effect on heat transport.

For both regimes, strong, systematic, large-scale flows can be driven but they vary significantly in their character depending on the rotational constraint. In regime (i), if the rotation vector is tilted from the vertical, then a systematic mean flow (with vertical shear) is driven; here the mean is taken over horizontal planes. Stratification has the effect of “asymmetrizing” the mean flow so that it is no longer symmetric about the mid depth. The addition of stratification can (in cases that start out with a nonzero vertically integrated horizontal momentum) also introduce a symmetry breaking that leads to a net spiraling of the mean flow, not seen in the Boussinesq system (even when the system is initialized with a state that has a nonzero vertically integrated horizontal momentum). In regime (ii), the systematic flows take the form of coherent structures, which can correspond to a large-scale vortex. For a fixed Rossby number at the bottom of the domain, the stratification has the effect of increasing Ro (decreasing the rotational constraint) as one moves upward in the layer. This coincides with larger (than in the Boussinesq case) departures from a Taylor–Proudman state and also the loss of a coherent vortex near the top of the domain, owing to modification of the energy transfer mechanisms.

Despite the simplicity of the model considered here, some of the underlying physics, e.g., the role of stratification in modifying convection, may still be relevant in many astrophysical contexts. It is interesting to speculate on the implications of our results for large-scale structures in giant planets. We believe that the effect of stratification here is to disrupt large-scale vortex structures at rapid rotation, owing to changes in the Rossby number across the convective structure. However, it is unclear what the coherence of the vortex would be in (more rapidly rotating) cases where the Rossby number remains small for the whole structure. Hence we are wary of overstating the implication of these calculations for the vortices found in Jupiter and Saturn at this stage.

We also note that shear is expected to play an important role in the generation of a magnetic field through dynamo action. In addition, helicity is thought to be important for the generation of a large-scale magnetic field. For both regimes considered here, there is significant helicity in the layer and the key difference introduced by stratification is that the flows now possess net helicity. However, the net helicity for the cases considered here is still relatively small and so it remains to be seen if this helps in the generation of dynamo waves at high magnetic Reynolds number Rm . This suggests that the next step should involve the investigation of the dynamo properties of flows such as those examined here.

ACKNOWLEDGMENTS

The authors would like to acknowledge two anonymous referees for helpful and constructive reviews of the initial manuscript. L.K.C. acknowledges support from STFC Grant No. ST/R000891/1 and the European Research Council under ERC Grant Agreement No. 337705 (CHASM). S.M.T. would like to acknowledge support of funding from the European Research Council under the European Union Horizon 2020 research and innovation program (Grant Agreement No. D5S-DLV-786780). The calculations for this paper were performed on the University of Exeter Supercomputer, Isca, part of the University of Exeter High-Performance Computing facility. Additional simulations were performed using the DiRAC Data Intensive service at Leicester, operated by the University of Leicester IT Services, which forms part of the STFC DiRAC HPC Facility. This equipment was funded by BEIS capital funding via STFC Capital Grants No. ST/K000373/1 and No. ST/R002363/1 and STFC DiRAC Operations Grant No. ST/R001014/1. DiRAC is part of the National e-Infrastructure. The 3D renderings in Figs. 3, 7, and 9 were created using VAPOR [80].

-
- [1] J. Schou, H. M. Antia, S. Basu, R. S. Bogart, R. I. Bush, S. M. Chitre, J. Christensen-Dalsgaard, M. P. Di Mauro, W. A. Dziembowski, A. Eff-Darwich *et al.*, Helioseismic studies of differential rotation in the solar envelope by the solar oscillations investigation using the Michelson Doppler imager, *Astrophys. J.* **505**, 390 (1998).
- [2] C. C. Porco, R. A. West, A. McEwen, A. D. Del Genio, A. P. Ingersoll, P. Thomas, S. Squyres, L. Dones, C. D. Murray, T. V. Johnson *et al.*, Cassini imaging of Jupiter’s atmosphere, satellites, and rings, *Science* **299**, 1541 (2003).
- [3] A. R. Vasavada and A. P. Showman, Jovian atmospheric dynamics: An update after Galileo and Cassini, *Rep. Prog. Phys.* **68**, 1935 (2005).
- [4] A. Adriani, A. Mura, G. Orton, C. Hansen, F. Altieri, M. Moriconi, J. Rogers, G. Eichstädt, T. Momary, A. P. Ingersoll *et al.*, Clusters of cyclones encircling Jupiter’s poles, *Nature (London)* **555**, 216 (2018).
- [5] G. K. Vallis, *Atmospheric and Oceanic Fluid Dynamics: Fundamentals and Large-Scale Circulation* (Cambridge University Press, Cambridge, 2006).
- [6] N. H. Brummell and J. Hart, High Rayleigh number β -convection, *Geophys. Astrophys. Fluid Dyn.* **68**, 85 (1993).
- [7] E. Grote and F. Busse, Dynamics of convection and dynamos in rotating spherical fluid shells, *Fluid Dyn. Res.* **28**, 349 (2001).
- [8] J. Rotvig and C. A. Jones, Multiple jets and bursting in the rapidly rotating convecting two-dimensional annulus model with nearly plane-parallel boundaries, *J. Fluid Mech.* **567**, 117 (2006).
- [9] A. S. Brun and J. Toomre, Turbulent convection under the influence of rotation: Sustaining a strong differential rotation, *Astrophys. J.* **570**, 865 (2002).
- [10] M. S. Miesch, Large-scale dynamics of the convection zone and tachocline, *Living Rev. Solar Phys.* **2**, 1 (2005).
- [11] L. L. Kitchatinov and G. Rüdiger, Differential rotation in solar-type stars: Revisiting the Taylor-number puzzle, *Astron. Astrophys.* **299**, 446 (1995).
- [12] M. Rempel, Influence of random fluctuations in the λ -effect on meridional flow and differential rotation, *Astrophys. J.* **631**, 1286 (2005).
- [13] S. Tobias, K. Dagon, and J. Marston, Astrophysical fluid dynamics via direct statistical simulation, *Astrophys. J.* **727**, 127 (2011).
- [14] S. M. Tobias and J. B. Marston, Direct Statistical Simulation of Out-of-Equilibrium Jets, *Phys. Rev. Lett.* **110**, 104502 (2013).
- [15] J. B. Marston, G. P. Chini, and S. M. Tobias, Generalized Quasilinear Approximation: Application to Zonal Jets, *Phys. Rev. Lett.* **116**, 214501 (2016).
- [16] M. S. Miesch, J. R. Elliott, J. Toomre, T. L. Clune, G. A. Glatzmaier, and P. A. Gilman, Three-dimensional spherical simulations of solar convection. I. Differential rotation and pattern evolution achieved with laminar and turbulent states, *Astrophys. J.* **532**, 593 (2000).
- [17] J. R. Elliott, M. S. Miesch, and J. Toomre, Turbulent solar convection and its coupling with rotation: The effect of Prandtl number and thermal boundary conditions on the resulting differential rotation, *Astrophys. J.* **533**, 546 (2000).
- [18] U. R. Christensen, Zonal flow driven by deep convection in the major planets, *Geophys. Res. Lett.* **28**, 2553 (2001).
- [19] U. R. Christensen, Zonal flow driven by strongly supercritical convection in rotating spherical shells, *J. Fluid Mech.* **470**, 115 (2002).
- [20] M. K. Browning, A. S. Brun, and J. Toomre, Simulations of core convection in rotating A-type stars: Differential rotation and overshooting, *Astrophys. J.* **601**, 512 (2004).
- [21] T. Gastine and J. Wicht, Effects of compressibility on driving zonal flow in gas giants, *Icarus* **219**, 428 (2012).
- [22] T. Gastine, J. Wicht, and J. M. Aurnou, Zonal flow regimes in rotating anelastic spherical shells: An application to giant planets, *Icarus* **225**, 156 (2013).
- [23] R. K. Yadav, T. Gastine, U. R. Christensen, L. Duarte, and A. Reiners, Effect of shear and magnetic field on the heat-transfer efficiency of convection in rotating spherical shells, *Geophys. J. Int.* **204**, 1120 (2015).

- [24] W. Dietrich, T. Gastine, and J. Wicht, Reversal and amplification of zonal flows by boundary enforced thermal wind, *Icarus* **282**, 380 (2017).
- [25] D. H. Hathaway and R. C. J. Somerville, Three-dimensional simulations of convection in layers with tilted rotation vectors, *J. Fluid Mech.* **126**, 75 (1983).
- [26] D. H. Hathaway and R. C. J. Somerville, Nonlinear interactions between convection, rotation and flows with vertical shear, *J. Fluid Mech.* **164**, 91 (1986).
- [27] D. H. Hathaway and R. C. J. Somerville, Thermal convection in a rotating shear flow, *Geophys. Astrophys. Fluid Dyn.* **38**, 43 (1987).
- [28] K. Julien and E. Knobloch, Strongly nonlinear convection cells in a rapidly rotating fluid layer: The tilted f -plane, *J. Fluid Mech.* **360**, 141 (1998).
- [29] N. Saito and K. Ishioka, Interaction between thermal convection and mean flow in a rotating system with a tilted axis, *Fluid Dyn. Res.* **43**, 065503 (2011).
- [30] L. K. Currie and S. M. Tobias, Mean flow generation in rotating anelastic two-dimensional convection, *Phys. Fluids* **28**, 017101 (2016).
- [31] L. K. Currie and S. M. Tobias, Convection-driven kinematic dynamos with a self-consistent shear flow, *Geophys. Astrophys. Fluid Dyn.* **113**, 131 (2019).
- [32] F. H. Busse, Thermal instabilities in rapidly rotating systems, *J. Fluid Mech.* **44**, 441 (1970).
- [33] C. A. Jones, J. Rotvig, and A. Abdulrahman, Multiple jets and zonal flow on jupiter, *Geophys. Res. Lett.* **30**, 1731 (2003).
- [34] S. M. Tobias, J. S. Oishi, and J. B. Marston, Generalized quasilinear approximation of the interaction of convection and mean flows in a thermal annulus, *Proc. R. Soc. A* **474**, 20180422 (2018).
- [35] J. Boussinesq, *Théorie Analytique de la Chaleur: Mise en Harmonie avec la Thermodynamique et avec la Théorie Mécanique de la Lumière* (Gauthier-Villars, Paris, 1903), Vol. 2.
- [36] E. A. Spiegel and G. Veronis, On the Boussinesq approximation for a compressible fluid, *Astrophys. J.* **131**, 442 (1960).
- [37] A. Anufriev, C. Jones, and A. Soward, The Boussinesq and anelastic liquid approximations for convection in the Earth's core, *Phys. Earth Planet. Interiors* **152**, 163 (2005).
- [38] M. French, A. Becker, W. Lorenzen, N. Nettelmann, M. Bethkenhagen, J. Wicht, and R. Redmer, *Ab initio* simulations for material properties along the Jupiter adiabat, *Astrophys. J. Suppl. Ser.* **202**, 5 (2012).
- [39] L. D. Duarte, J. Wicht, and T. Gastine, Physical conditions for Jupiter-like dynamo models, *Icarus* **299**, 206 (2018).
- [40] J. Christensen-Dalsgaard, W. Däppen, S. Ajukov, E. Anderson, H. Antia, S. Basu, V. Baturin, G. Berthomieu, B. Chaboyer, S. Chitre *et al.*, The current state of solar modeling, *Science* **272**, 1286 (1996).
- [41] E. N. Parker, in *Physics of Space: Growth Points and Problems*, edited by N. Meyer-Vernet, M. Moncuquet, and F. Pantellini (Springer, Dordrecht, 2001), pp. 1–11.
- [42] E. H. Anders and B. P. Brown, Convective heat transport in stratified atmospheres at low and high mach number, *Phys. Rev. Fluids* **2**, 083501 (2017).
- [43] L. Novi, J. von Hardenberg, D. W. Hughes, A. Provenzale, and E. A. Spiegel, Rapidly rotating Rayleigh-Bénard convection with a tilted axis, *Phys. Rev. E* **99**, 053116 (2019).
- [44] L. K. Currie, The driving of mean flows by convection, Ph.D. thesis, University of Leeds, 2014.
- [45] N. H. Brummell, N. E. Hurlburt, and J. Toomre, Turbulent compressible convection with rotation. I. Flow structure and evolution, *Astrophys. J.* **473**, 494 (1996).
- [46] N. H. Brummell, N. E. Hurlburt, and J. Toomre, Turbulent compressible convection with rotation. II. Mean flows and differential rotation, *Astrophys. J.* **493**, 955 (1998).
- [47] K. L. Chan, Rotating convection in f -planes: Mean flow and Reynolds stress, *Astrophys. J.* **548**, 1102 (2001).
- [48] T. M. Rogers and G. A. Glatzmaier, Penetrative convection within the anelastic approximation, *Astrophys. J.* **620**, 432 (2005).
- [49] T. M. Rogers, G. A. Glatzmaier, and S. E. Woosley, Simulations of two-dimensional turbulent convection in a density-stratified fluid, *Phys. Rev. E* **67**, 026315 (2003).
- [50] J. Verhoeven and S. Stellmach, The compressional beta effect: A source of zonal winds in planets? *Icarus* **237**, 143 (2014).

- [51] M. Kessar, D. W. Hughes, E. Kersalé, K. A. Mizerski, and S. M. Tobias, Scale selection in the stratified convection of the solar photosphere, *Astrophys. J.* **874**, 103 (2019).
- [52] S. R. Lantz, Dynamical behavior of magnetic fields in a stratified, convecting fluid layer, Ph.D. thesis, Cornell University, 1992.
- [53] S. I. Braginsky and P. H. Roberts, Equations governing convection in Earth's core and the geodynamo, *Geophys. Astrophys. Fluid Dyn.* **79**, 1 (1995).
- [54] S. R. Lantz and Y. Fan, Anelastic Magnetohydrodynamic equations for modeling solar and stellar convection zones, *Astrophys. J.* **121**, 247 (1999).
- [55] K. A. Mizerski and S. M. Tobias, The effect of stratification and compressibility on anelastic convection in a rotating plane layer, *Geophys. Astrophys. Fluid Dyn.* **105**, 566 (2011).
- [56] G. A. Glatzmaier and P. A. Gilman, Compressible convection in a rotating spherical shell. IV-Effects of viscosity, conductivity, boundary conditions, and zone depth, *Astrophys. J. Suppl. Ser.* **47**, 103 (1981).
- [57] C. A. Jones and K. M. Kuzanyan, Compressible convection in the deep atmospheres of giant planets, *Icarus* **204**, 227 (2009).
- [58] <http://dedalus-project.org>.
- [59] K. J. Burns, G. M. Vasil, J. S. Oishi, D. Lecoanet, and B. P. Brown, Dedalus: A flexible framework for numerical simulations with spectral methods, *Phys. Rev. Res.* **2**, 023068 (2020).
- [60] S. Kato and W. Unno, Convective instability in polytropic atmospheres, II, *Publ. Astron. Soc. Jpn.* **12**, 427 (1960).
- [61] C. A. Jones, P. H. Roberts, and D. J. Galloway, Compressible convection in the presence of rotation and a magnetic field, *Geophys. Astrophys. Fluid Dyn.* **53**, 145 (1990).
- [62] M. A. Calkins, K. Julien, and P. Marti, Onset of rotating and non-rotating convection in compressible and anelastic ideal gases, *Geophys. Astrophys. Fluid Dyn.* **109**, 422 (2015).
- [63] R. Long, J. Mound, C. Davies, and S. Tobias, Scaling behavior in spherical shell rotating convection with fixed-flux thermal boundary conditions, *J. Fluid Mech.* **889**, A7 (2020).
- [64] M. J. Mantere, P. J. Käpylä, and T. Hackman, Dependence of the large-scale vortex instability on latitude, stratification, and domain size, *Astron. Nachr.* **332**, 876 (2011).
- [65] K. L. Chan and H. G. Mayr, Numerical simulation of convectively generated vortices: Application to the Jovian planets, *Earth Planet. Sci. Lett.* **371-372**, 212 (2013).
- [66] A. M. Rubio, K. Julien, E. Knobloch, and J. B. Weiss, Upscale Energy Transfer in Three-Dimensional Rapidly Rotating Turbulent Convection, *Phys. Rev. Lett.* **112**, 144501 (2014).
- [67] B. Favier, L. Silvers, and M. Proctor, Inverse cascade and symmetry breaking in rapidly rotating Boussinesq convection, *Phys. Fluids* **26**, 096605 (2014).
- [68] C. Guervilly, D. W. Hughes, and C. A. Jones, Large-scale vortices in rapidly rotating Rayleigh-Bénard convection, *J. Fluid Mech.* **758**, 407 (2014).
- [69] B. Favier, C. Guervilly, and E. Knobloch, Subcritical turbulent condensate in rapidly rotating Rayleigh-Bénard convection, *J. Fluid Mech.* **864**, R1 (2019).
- [70] C. Jones, D. Moore, and N. Weiss, Axisymmetric convection in a cylinder, *J. Fluid Mech.* **73**, 353 (1976).
- [71] R. Clever and F. Busse, Low-Prandtl-number convection in a layer heated from below, *J. Fluid Mech.* **102**, 61 (1981).
- [72] A. Ribeiro, G. Fabre, J.-L. Guermond, and J. Aurnou, Canonical models of geophysical and astrophysical flows: Turbulent convection experiments in liquid metals, *Metals* **5**, 289 (2015).
- [73] See Supplemental Material at <http://link.aps.org/supplemental/10.1103/PhysRevFluids.5.073501> for movies corresponding to the mean flows discussed in Sec. III B 1 and visualized in Fig. 6.
- [74] L. K. Currie, A. J. Barker, Y. Lithwick, and M. K. Browning, Convection with misaligned gravity and rotation: Simulations and rotating mixing length theory, *Mon. Not. R. Astron. Soc.* **493**, 5233 (2020).
- [75] A. Alexakis, P. D. Mininni, and A. Pouquet, Shell-to-shell energy transfer in magnetohydrodynamics. I. steady state turbulence, *Phys. Rev. E* **72**, 046301 (2005).

- [76] K. Moffatt and E. Dormy, *Self-Exciting Fluid Dynamos* (Cambridge University Press, Cambridge, 2019), Vol. 59.
- [77] F. Cattaneo and S. Tobias, On large-scale dynamo action at high magnetic Reynolds number, [Astrophys. J. **789**, 70 \(2014\)](#).
- [78] G. Nigro, P. Pongkitiwanchakul, F. Cattaneo, and S. Tobias, What is a large-scale dynamo? [Mon. Not. R. Astron. Soc. Lett. **464**, L119 \(2017\)](#).
- [79] P. Pongkitiwanchakul, G. Nigro, F. Cattaneo, and S. Tobias, Shear-driven dynamo waves in the fully nonlinear regime, [Astrophys. J. **825**, 23 \(2016\)](#).
- [80] S. Li, S. Jaroszynski, S. Pearce, L. Orf, and J. Clyne, VAPOR: A visualization package tailored to analyze simulation data in earth system science, [Atmosphere **10**, 488 \(2019\)](#).